Powder Technology 411 (2022) 117957

Contents lists available at ScienceDirect

Powder Technology

journal homepage: www.journals.elsevier.com/powder-technology

Understanding surface roughness on vertical surfaces of 316 L stainless steel in laser powder bed fusion additive manufacturing

Tianyu Zhang, Lang Yuan *

Department of Mechanical Engineering, University of South Carolina, Columbia, SC 29201, USA

HIGHLIGHTS

- Vertical surface roughness is positively correlated to melt pool width and depth.
- Powder and melt tracks dominate vertical surface roughness at low energy densities.
- The dross dominates vertical surface roughness at high energy densities.
- Inhomogeneous thermal distribution and melt pool instability drive dross formation.

GRAPHICAL ABSTRACT

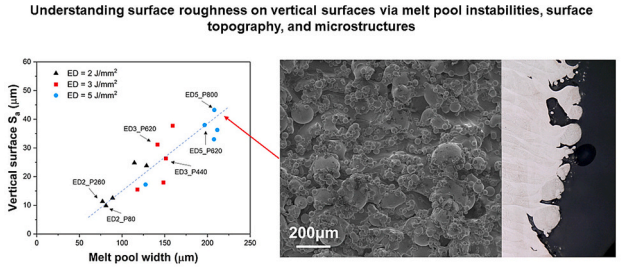

- The large-sized dross dominates the surface roughness on vertical surfaces at high energy density conditions.
- The dross formation is a multiple-layer process associated with the inhomogeneous thermal distribution and the melt pool instability.

ARTICLE INFO

Keywords:
Laser powder bed fusion
Surface roughness
Melt pool instability
Dross formation
Microstructure

ABSTRACT

Laser powder bed fusion (L-PBF) offers high degrees of freedom to create complex geometries with fine features. Controlling surface roughness is one of the means of improving mechanical and functional properties. This is critical for those surfaces that post-treatments cannot process. This study investigated the effects of a wide range of processing parameters grouped by energy density on surface roughness, particularly at vertical surfaces in L-PBF. The surface arithmetic average roughness, Sa, was measured via confocal microscopy. Scanning electron microscope was used to examine the detailed characteristics and the solidification microstructure on and near surfaces. Increasing laser power and speed under the identical energy density or increasing energy density under the equal speed results in rough vertical surfaces. Solidified melt tracks and partially remelted particles dominate the vertical surface roughness in cases with low energy densities. In contrast, the dross formation contributes to the high vertical surface roughness in cases with high energy densities. By examining the melt pool morphology and the solidification microstructure near the surfaces, the mechanism grounded on a multi-layer melt pool instability is proposed to explain the dominant factors for vertical surfaces. The insights into the formation of key surface characteristics can assist in designing process parameters and generating innovative methods to improve surface roughness.

* Corresponding author.
E-mail address: langyuan@cec.sc.edu (L. Yuan).

https://doi.org/10.1016/j.powtec.2022.117957
Received 9 July 2022; Received in revised form 8 September 2022; Accepted 16 September 2022
Available online 21 September 2022

1. Introduction

Laser Powder Bed Fusion (L-PBF) Additive Manufacturing (AM) combines precision powder bed formation for materials deposition with high-resolution local melting for direct material consolidation. The layer-by-layer approach inherits high degrees of design freedom and enables the production of complex geometries with potentially location-specific materials properties [1–3]. Significant progress has been made to understand the complex physics, which paves the path to ultimately control microstructures and defects, such as distortion, porosity, and cracking, for a wide range of metallic alloys in L-PBF [4–6]. However, the methods to achieve desired surface roughness that describes the surface topography of printed parts are still limited [7].

Surface roughness influences products' geometrical tolerances and plays a vital role in mechanical and functional properties [8,9]. For instance, the fatigue life of specimens with a rough surface can be approximately half of that with a smooth surface [10], where coarse surface features, e.g., the sharp radius of curvature or deep notch, can serve as stress concentration and fatigue crack initiation sites [11]. Functionally, surface characteristics can alternate the fluid flow behaviors, affecting the pressure drop in printed mini-channels and significantly influencing the heat transfer properties [12,13]. Although various post-process techniques can be applied to retreat the surfaces, e.g., machining, shot peening, and chemical processing [14], inner surfaces within a complex geometry are still difficult to be processed, limiting the part performance due to undesired surface roughness. The formation of surface topography in L-PBF owns to the complex and intertwined network of cause-effect relationships between the physical phenomena, e.g., heat transfer, solidification, fluid dynamics and surface tension [15], and process parameters, e.g., powder size distribution, laser parameters, layer thickness and scanning pattern [16–25]. It has been generally agreed that the surface roughness was contributed by partially remelted particles, spatter particles, and balling effects besides the geometrical stepping effects [26,27].

Prior studies have revealed qualitative correlations between laser process parameters and the surface roughness for different materials systems [28–31]. However, the majority of the studies evaluated the roughness on the top surfaces via printed tracks or cubic samples. Gu et al. [32] studied both tracks and blocks for 316 L stainless stress with L-PBF. They found that increasing the volumetric density of energy input by lowering scan speed, increasing laser power, or decreasing powder layer thickness, decreased the tendency of balling, which is governed by the wetting/surface tension characteristic of the melt pool, powder, and the solidified surface, resulting in low surface roughness. Yadroitsev et al. [33] investigated single tracks of 304 L and 904 L stainless steel. Their results indicated that instability zones appeared both at low scanning speed as the form of irregularities and at high scanning speed due to the balling effect. Calignano et al. [34] concluded that the scanning speed had the most influence on surface roughness for AlSi10Mg. Yang et al. [35] reached similar conclusions for Ti-6Al-4V, where scanning speed dominated the instability, followed by laser power and layer thickness. Chen et al. illustrated that the large size powder particles result in a coarse surface roughness finish [21]. Qiu et al. [22] explained that the high layer thickness led to a high porosity level with the irregularly shaped melt pool track and cave-shaped pores on the top surface, which degraded the surface quality. Shi et al. [23] concluded that the high layer thickness mainly deteriorated the surface quality other than density and tensile properties. Alfieri et al. [25] verified that the wobbling scanning strategy is helpful in improving surface topography, compared with linear scanning processing due to lower heat effects in the base metal.

Limited studies have explored the roughness on vertical and angled surfaces. Mumtaz et al. [36] showed that vertical surface roughness on Inconel 625 was reduced with increasing laser power via enhanced wettability of the melt. Meanwhile, reduced scan speed increased roughness. Yang et al. [37] studied the linear energy density on vertical surface roughness for AlSi10Mg cubes and drew similar conclusions. They showed that the surface roughness could be reduced by approximately 70% by controlling the energy density. Higher energy density could cause instability of deposited tracks due to the stronger Marangoni convention and metal evaporation, resulting in increased surface roughness. Yang et al. [38] studied the impact of process parameters on the surface roughness of surfaces with 30^{o}, $45^{o,}$ and 60^{o} inclined angles and confirmed that the dominant factor was contour scanning speed. Han et al. [39] discussed the impact of scanning speed and hatch spacing on inclined AlSi10Mg with 45^{o} inclined angle. The infiltration effect explained the higher scanning speed and hatch spacing led to the lower surface roughness, where the liquid infiltrates into the gap between powders on the inclined surface and reduces the surface roughness via the formation of dross. Similar conclusions were drawn by Tian et al. [24] that low laser contour scan power could provide a better down-facing finish surface quality combined with skywriting mode by achieving a more stable melt track and smoothing the surface. Charles et al. [40] further explained the dross formation, which dominated the dimensional inaccuracy and surface roughness at down-facing surfaces. They concluded through numerical simulation that dross formation was primarily caused by high energy density via the drilling effect without mechanical resistance of the underlying powder domain [41]. Although the dominant surface characteristics [42], including balling, spatter particles, and partially remelted particles, have been observed, the underlying mechanisms are still under investigation for vertical surfaces.

In this study, cubic samples fabricated by L-PBF with a wide range of laser power and speed, grouped by energy density, were examined by optical microscope and scanning electron microscope (SEM) for surface topography, melt pool dimensions, and microstructure characteristics to interpret the surface roughness. Melt pool instability, partially remelted particles, spatters and dross formation were discussed, which led to new insights into understanding the as-printed vertical surfaces in L-PBF.

2. Methodology

Commercial gas atomized 316 L stainless steel powder supplied by Carpenter Technology Cooperation with a particle size distribution from 15 to 45 μm with a mean size of 30 μm was used in this study. The nominal composition of the powder is listed in Table 1. The powder particles exhibit spherical morphology via SEM, and few are with satellites, as shown in Fig. 1. Cubic samples with a size of 10 mm × 10 mm × 10 mm were printed to study the surface characteristics of both top and vertical surfaces under different energy densities. The L-PBF machine, Aconity MIDI, which equips a single-mode fiber laser with a maximum laser of 1000 W, was utilized to print those samples in the argon environment. During the printing, the oxygen level in the chamber was controlled to be lower than 100 ppm to minimize oxidation. Three groups of experiments with a total of 15 samples at energy densities of 2 J/mm^2, 3 J/mm^2, 5 J/mm^2 were studied. Each group has two repeats to ensure repeatability. Note that the energy density (ED) in this study is defined as

$$ED = \frac{P}{V \times H} \tag{1}$$

where P is the laser power, V is the laser scanning speed, and H is the hatch spacing.

The focus of this study is on the relationship between surface roughness and laser processing parameters. The laser spot size and hatch spacing were set at 100 μm for all prints. The layer thickness remains constant at 30 μm. In each group, the laser power was chosen as 80 W, 260 W, 440 W, 620 W, and 800 W, with the scanning speed ranging from 160 mm/s to 4000 mm/s, plotted in Fig. 2. The samples are named E*_P* in this study for simplification. For example, E2_P80 presents that the energy density equals 2 J/mm^2 and the power is 80 W, which gives the speed of 400 mm/s based on Eq.(1). The selection of parameters ensures

Table 1
The nominal chemical composition (wt%) of stainless steel 316 L.

Element	Fe	Ni	Cr	O	Si	S	P	N	C	Mo	Mn	Cu
Wt%	Bal.	12.7	17.7	0.03	0.62	0.005	0.007	0.10	0.022	2.36	0.65	0.02

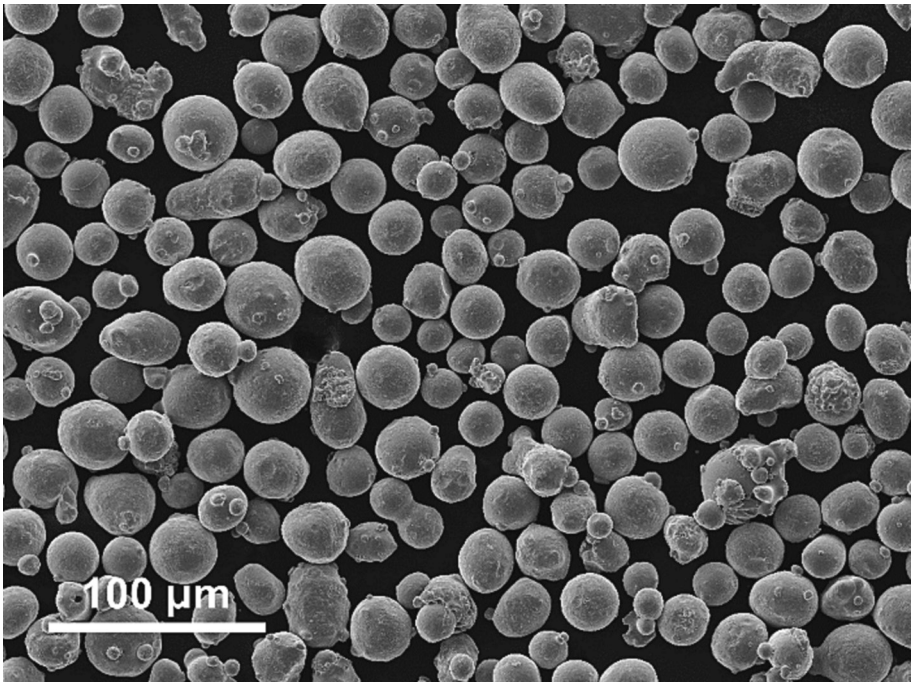

Fig. 1. Particle morphologies via SEM for the stainless steel 316 L powder.

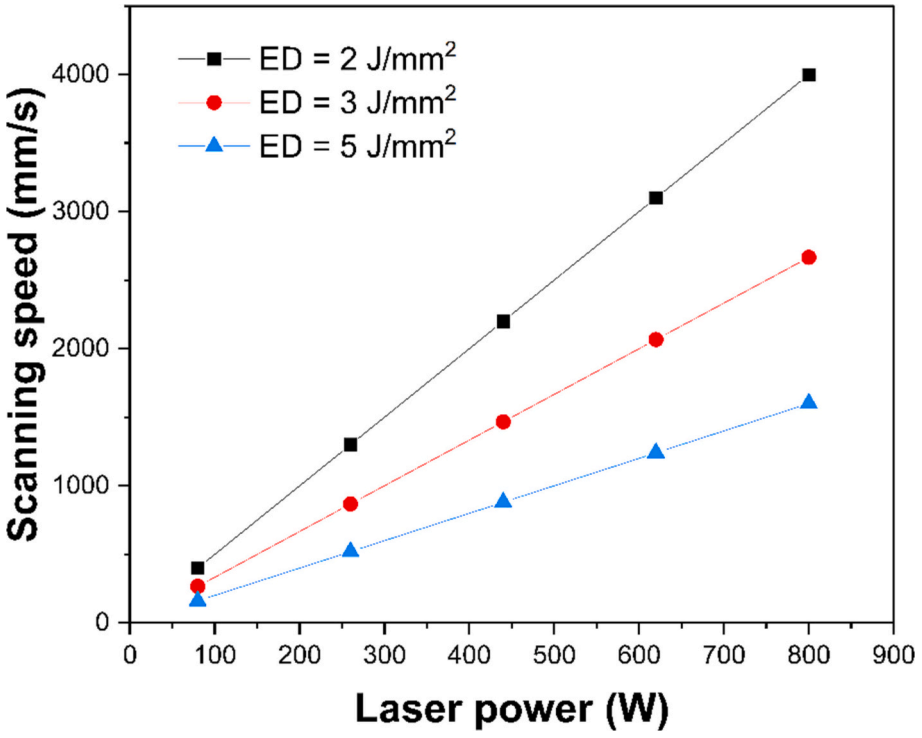

Fig. 2. Process parameters grouped by energy density.

a wide range of laser power and speed without significant keyholing [43]. In addition, the process conditions with high laser power of >400 W haven't been widely investigated in L-PBF. Note that the surface energy density in the cases can be translated to the volumetric energy density by considering the layer thickness (Th), defined as $\frac{P}{V\times H\times Th}$ in other studies. Thus, the range of energy density in this study would be from 66.7 to 166.7 J/mm^3, which covers the practical parametric space for production [44,45]. A simple hatching scanning strategy was applied with 90 degrees of rotation between layers. One contour scan was performed on each layer with the same parameters as the hatches.

The surface topography of each sample was obtained via Keyence VHX-5000 digital optical microscope and Tescan Vega3 SEM. The height information $Z(x,y)$ was captured in the digital Keyence microscope to examine the surface roughness. Sa, the arithmetical mean height of a surface, was employed to quantify the surface roughness value. It is calculated by:

$$S_a = \frac{1}{A}\iint_A |z(x,y)|dxdy \quad (2)$$

Samples were cut in half by wire Electrical Discharge Machining (EDM) to evaluate the melt pool dimensions and the solidification microstructure. The cut plane is perpendicular to the laser scanning direction on the last layer. For metallurgical characterizations, the samples were ground, polished, and then etched with the mixture of 75 vol% of HCl and 25 vol% HNO_3 for 15 s. An example of the top surface after etching is shown in Fig. 3(a), where the melt pool width and depth were extracted at multiple locations on two repeats. The melt pool width was also measured from the top-down view images to confirm the measurement further, as shown in Fig. 3(b). SEM images were taken to reveal both the surface characteristics and the microstructure with sub-grain features, which assist in understanding and illustrating the mechanisms that drive surface roughness.

3. Results and discussion

3.1. Melt pool morphology and surface roughness at the top surfaces

Fig. 4 shows the melt pool width and depth versus the laser power under different energy densities. The ratio of melt pool width to the melt pool depth is measured to be between 1.85 and 3.51, which indicates that the laser fabrication model is towards thermal conduction [43]. Under the same laser power, the higher the energy density, the larger the melt pool width and depth. This is because the lower laser scanning speed allows more energy to be absorbed during fabrication. Under the same energy density, the general behavior is that the higher the laser power or speed, the larger the melt pool size dimensions, which is consistent with prior observations [46]. With the same energy density delivered to the fabricated part, the higher scanning speed offers less time for the heat to be diffused or dispersed away and leads to a larger melt pool size, assuming the energy does not vary significantly under the same energy density.

Fig. 5 shows the melt pool morphologies on the top surface under different energy densities. At the low energy density (2 J/mm^2), the melt pool is relatively shallow and small. The connecting area between the melt pool and the powder is insufficient to provide a good wetting condition. Thus, surface tension brings the melt pool towards balling [47], shown in Fig. 5(a) and (c). Since the width is comparable to the hatch spacing, pores due to the lack of fusion defects are observed in Fig. 5(a). While under the high energy density (5 J/mm^2), shown in Fig. 5(b) and (d), the melt pool is relatively wide and deep with the increased laser power. The wider melt pool wets well with the powder and solidified tracks and leads to a flat top surface. Since the hatching space is 100 μm, part of the melt pool (width higher than 200 μm) will be remelted by the next track, further smoothing the top surface. On the other hand, the Marangoni force due to surface tension gradient can affect the flow direction in the melt pool, thus, the melt pool size. For 316 L stainless steel, when the sulfur level is lower than 75 ppm and the oxygen level remains lower than 570 ppm [48,49], the surface tension coefficient is a negative value, which means that the Marangoni flow is centrifugal outwards. In this study, the sulfur and oxygen compositions in the powder are relatively low (Table 1) at 50 ppm and 300 ppm, and the oxygen level in the chamber is lower than 100 ppm during the printing. This suggests that the Marangoni flow tends to widen the melt pool. With higher energy density, the high thermal gradient leads to a more robust centrifugal Marangoni flow, further assisting in flatting the top surface. In addition, a larger melt pool volume requires a longer cooling time, and gravity also helps reduce the curvature at the top surface [50].

Fig. 6 shows the top surface roughness Sa versus the laser power under different energy densities. In the high energy density group (5 J/mm^2), the top surface roughness decreases with the power and speed increase. However, in the low energy density group (2 J/mm^2), It behaves differently, showing a tendency to increase with increasing the laser power. With the intermediate energy group (3 J/mm^2), the surface roughness lies between the other two groups.

It has been reported that the roughness on the top surfaces is highly correlated to the melt pool size and the melt pool instability [51,52]. Under the low energy density condition of 2 J/mm^2, the melt tracks tend to be discontinuous due to insufficient wetting under small melt pool sizes. The melt pool becomes unstable with increasing speed. As measured in Fig. 7(a) and (b), the tail angle (by linking the end point of the melt pool to the widest two points of the melt pool) in ED2_P80 is approximately 60°, which is higher than ~45° in ED2_P800. This means that the melt pool length to width ratio increases with the increasing scanning speed, which further promotes the tendency for the melt pool to gather as discontinuous tracks, known as the Raleigh instability, commonly leading to balling [51]. These factors explain why the top surface roughness increases with the power/speed increases at energy density = 2 J/mm^2 conditions. While under high energy density condition of 5 J/mm^2, seen in Fig. 7(c) and (d), once the laser power (speed) increases, the melt pool size becomes more prominent with significant overlapping with the previous track, reducing the top surface roughness.

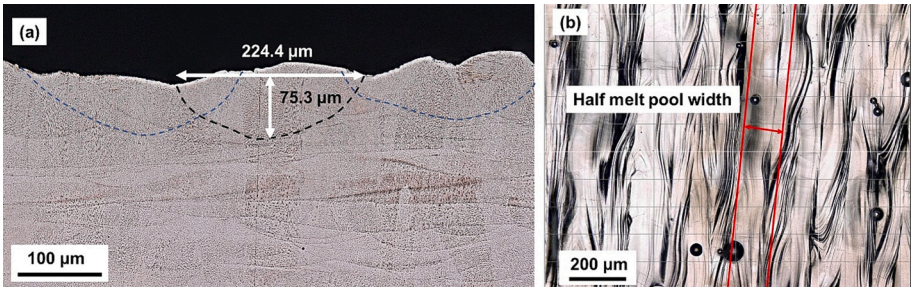

Fig. 3. Measurement of melt pool size from sample ED5_P800 (800 W 1600 mm/s): (a) depth and width from the cross-sectional view, and (b) half width from the top-down view.

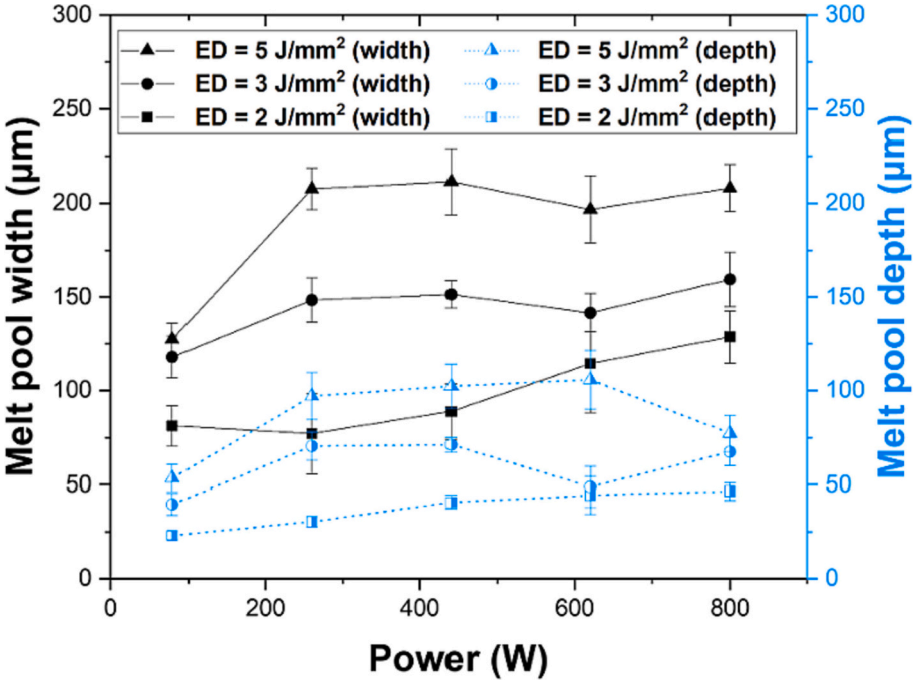

Fig. 4. Melt pool width and depth measured from the printed cubic samples.

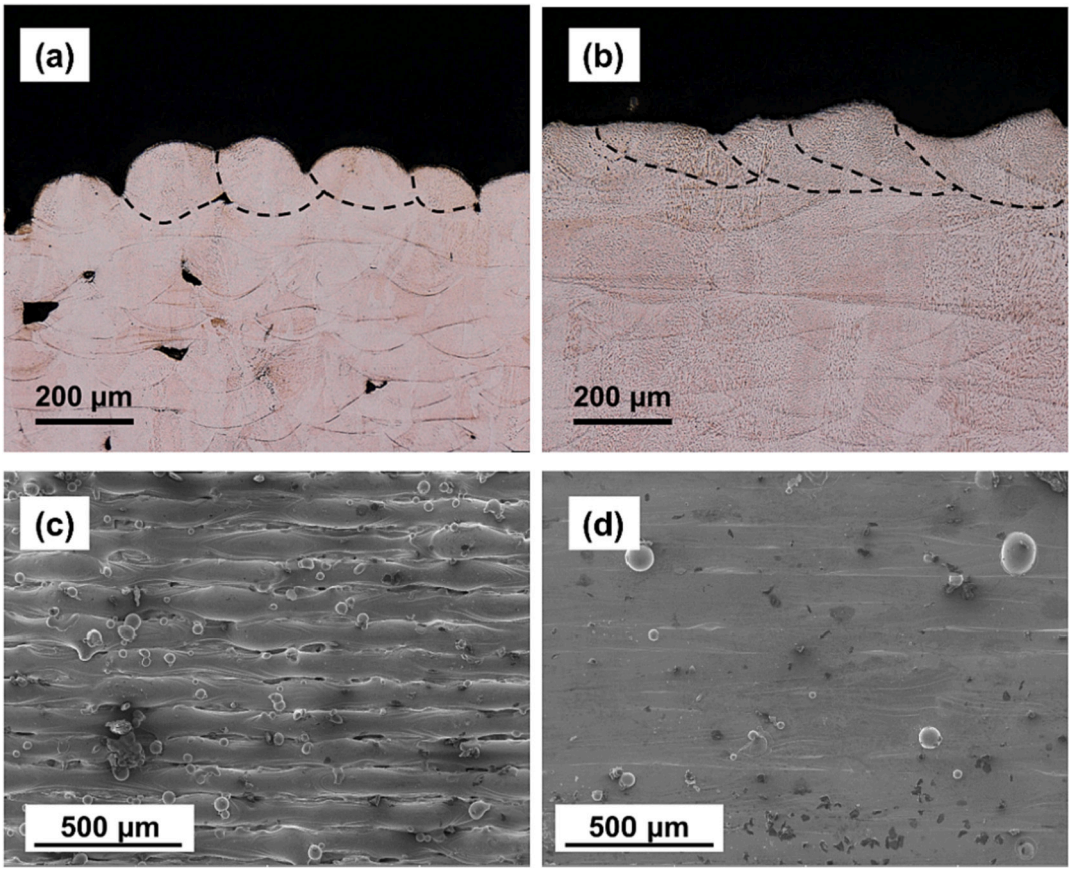

Fig. 5. Surface characteristics: (a) & (b) cross-section view for melt pool morphology, and (c) & (d) top-down view of top surfaces. (a) and (c) ED2_P260 (260 W 1300 mm/s), (b) and (d) ED5_P800 (800 W 1600 mm/s).

Meanwhile, with increased cooling time, Marangoni flow and gravity work against the surface tension to flatten the top surface. This explains the top Sa decreases with increasing the laser power and speed under high energy density conditions. Based on the current datasets and the analysis, it suggests that the L-PBF processing parameters of an energy density of minimal 5 J/mm^2 with laser power over 260 W can result in

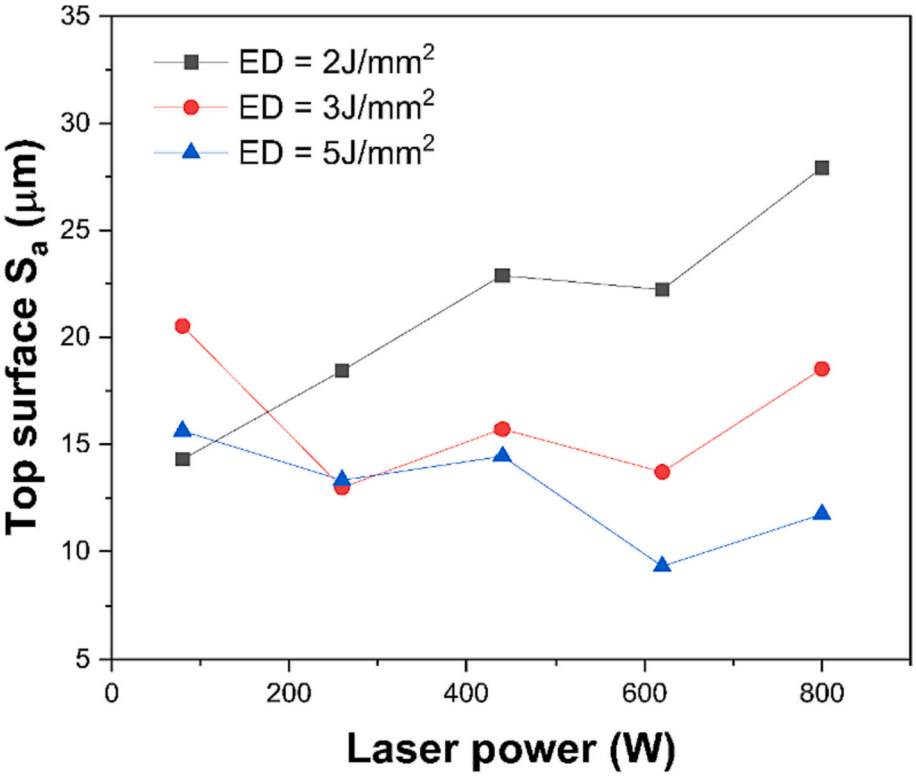

Fig. 6. Sa values for top surfaces.

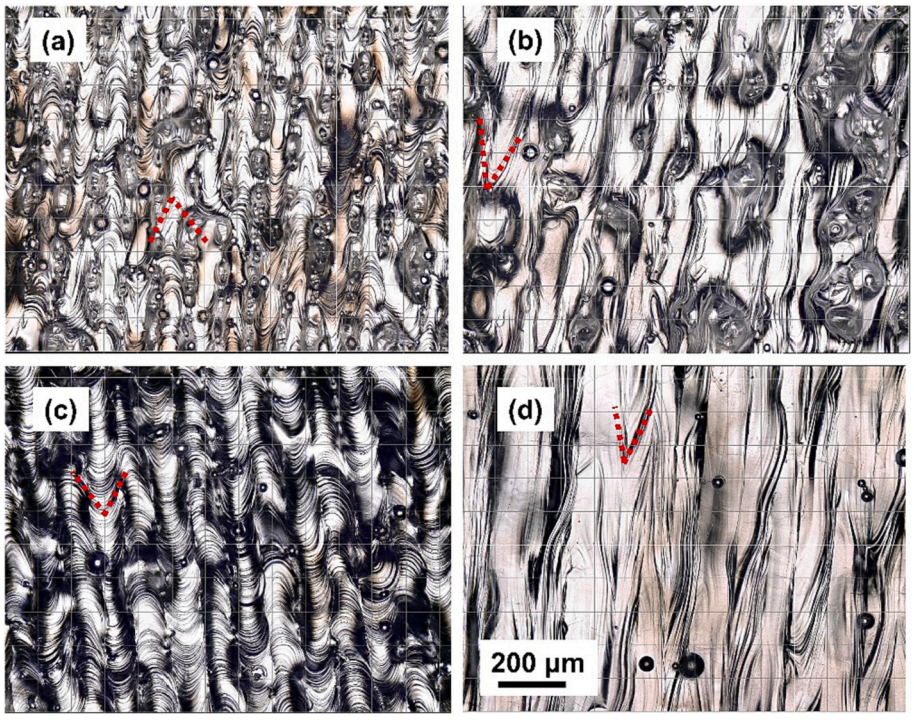

Fig. 7. Optical micrographs for top surfaces: (a) ED2_P80 (80 W 400 mm/s), Sa = 14.30 μm, (b) ED5_ 80 (80 W 160 mm/s), Sa = 27.93 μm, (c) ED2_P800 (800 W 4000 mm/s), Sa = 15.63 μm, and (d) ED5_800 (800 W 1600 mm/s), Sa = 11.74 μm.

better top surface quality (e.g., Sa < 15 μm). Note that the upper bound of the energy density is not explored here due to the potential of key-holing. In addition, the increase in the speed may increase the melt pool instability, although the melt pool width is also enlarged. Overall, the laser power of 800 W and speed of 1600 mm/s yields the best top surface quality in this study.

3.2. *Melt pool morphology and surface roughness at the vertical surfaces*

Fig. 8 shows the relationship between the Sa of vertical surfaces and

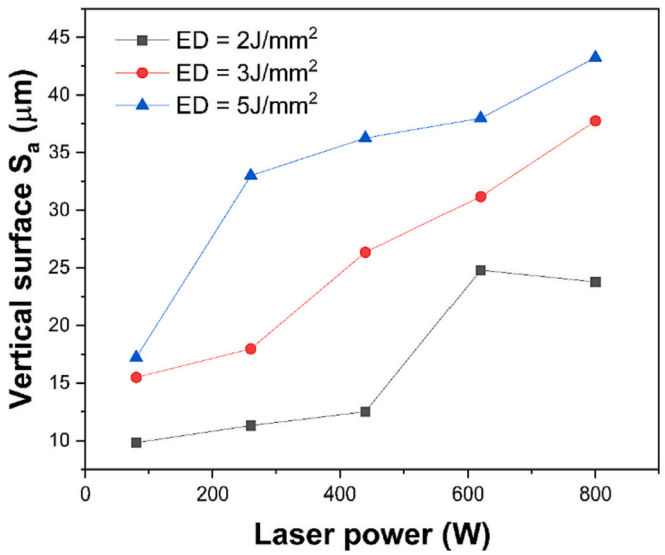

Fig. 8. Sa values for vertical surfaces.

laser power under different energy densities. Under the same energy density, the higher the laser power and speed, the coarser the roughness of vertical surfaces. Meanwhile, the higher the energy density (which also means lower speed) under the same laser power, the rougher the vertical surface. This suggests that the high energy density parameters lead to rough vertical surfaces, and the low energy density parameters result in better vertical surface finishing. The similarity was found in the trends shown in Fig. 4 and Fig. 8, both vertical surface Sa and melt pool dimensions increase with energy density or power/speed increase under the same energy density. Thus, the relationship between melt pool dimensions and vertical surface roughness is chosen in this study to discuss the mechanisms that drive the roughness on vertical surfaces.

Fig. 9 plots the melt pool width and depth against the vertical surface roughness, respectively. It illustrates that the roughness is positively correlated to the melt pool width or depth: the larger the melt pool size (no matter the width or the depth), the coarser the vertical surface roughness. To examine the factors that drive the surface roughness, two conditions under each energy density group were selected to show the detailed characteristics of the vertical surfaces: ED2_P80 and ED2_P260 from the 2 J/mm^2 group, ED3_P440 and ED3_P620 from the 3 J/mm^2 group and ED5_P620 and ED5_P800 from the ED 5 J/mm^2. The conditions are also marked in Fig. 9.

The topography of vertical surfaces and etched sectional images at the vertical surfaces are acquired for chosen samples. Fig. 10 shows the contour plot for Z heights of the vertical surfaces. Similar features can be identified in each group. At the energy density of 2 J/mm^2 group, the average surface roughness for all samples is 16.44 μm, including 11.31 μm for ED2_P80 and 9.83 μm for ED2_P260. From Fig. 10(a) and (d), the distance between the highest point and lowest point in one peak (Za) is <160 μm and 107 μm, respectively. Besides one outstanding melt track shown in Fig. 10(d), the vertical surface is dominated by the clean solidified tracks and attached particles, similarly reported in [53]. At the energy density of 5 J/mm^2 group, the vertical surface roughness Sa has a mean value of 33.54 μm with a value of 37.98 μm for ED5_P620 and 43.24 μm for ED5_P800. Large semi-spheres are observed in Fig. 10(c) and (f). Their sizes are approximately 80–120 μm, much larger than the powder size (15–45 μm). Although the attached particles still exist, these semi-spheres dominate the surface roughness and make the Za in the high energy density group higher than 300 μm. At the energy density of 3 J/mm^2 group, from Fig. 10(b) and (e), a mixture of melt tracks, attached particles, and relatively small-sized semi-spheres are observed, resulting in average surface roughness of 25.75 μm for this group, including 26.35 μm for ED3_P440 and 31.18 μm for ED3_P620. The distinguishing features between the low and high energy density groups indicate that the dominant features of surfaces are transitioning from smooth melt tracks and attached powder particles to large-sized semi-spheres with increasing energy density. Based on the observations from Figs. 9 and 10, it suggests that low vertical surface roughness (e.g., Sa < 15 μm) can be achieved by adapting lower energy density (e.g., 2 J/mm^2) with relatively low laser power (e.g. 440 W in this study). Note that the selection of the process conditions has the precondition that the laser power can sufficiently melt the powder to allow solid binding between layers. As reducing the laser power and speed, the vertical surfaces may exhibit gaps between melt pool tracks, leading to worse surface roughness. In this study, the laser power of 80 W and speed of 160 mm/s yield the best surface roughness.

Characterizations are performed on representative samples to examine the causes behind the dominant features from each group, namely, ED2_P260, ED3_P620, and ED5_P800, which have a low Sa value of 9.83 μm, a median value of 31.18 μm, and a high value of 43.24 μm, respectively. Fig. 11 shows the images with high magnification of the vertical surfaces and the cross sections after the etching observed with SEM and optical microscope, respectively. Note that these samples are also shown in the second row of Fig. 10. Fig. 11(a) indicates mostly smooth solidified tracks with sparely distributed partially remelted particles under the low laser energy density. The melt tracks on the vertical surface maintained well-defined shapes under the surface

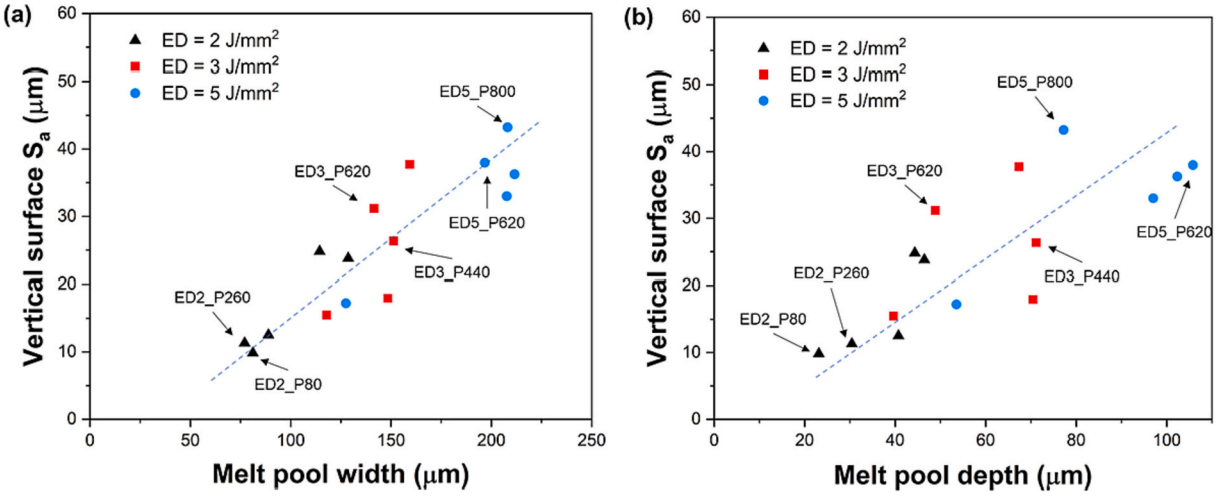

Fig. 9. Sa values for vertical surfaces: (a) against the melt pool width; and (b) against the melt pool depth.

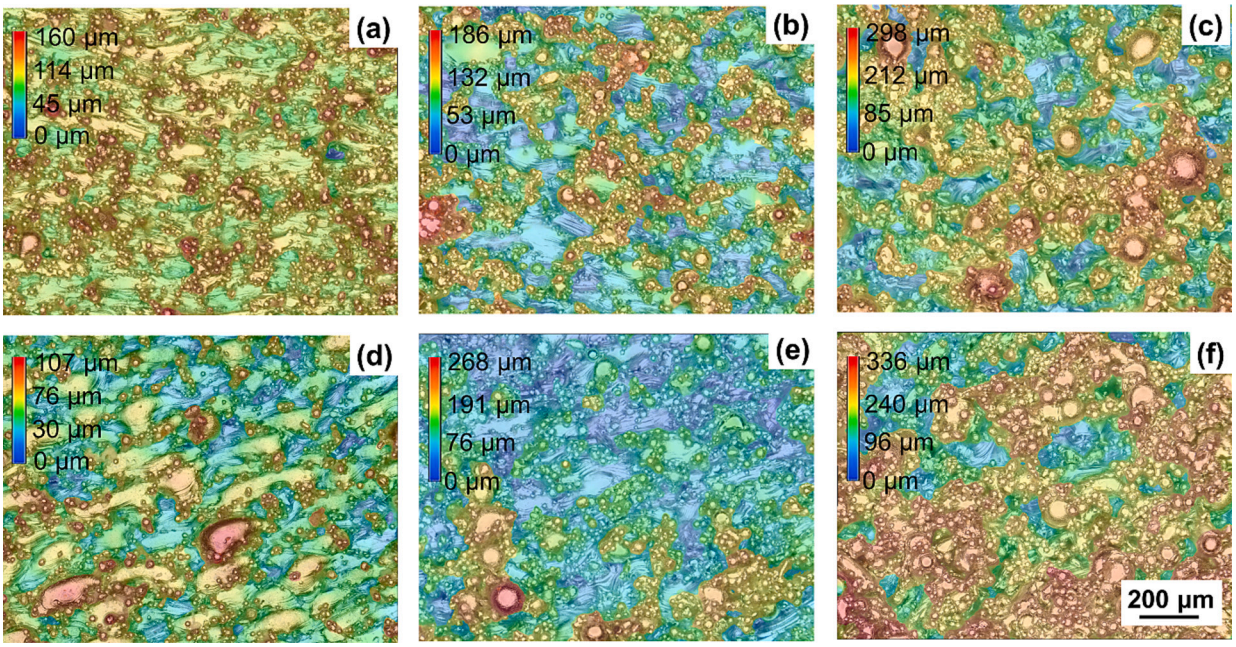

Fig. 10. Surface topography on vertical surfaces: (a) ED2_P80 (80 W 400 mm/s), (b) ED3_440 (440 W 1467 mm/s), (c) ED5_620 (620 W 1240 mm/s), (d) ED2_260 (260 W 1300 mm/s), (e) ED3_620 (620 W 2067 mm/s), and (f) ED5_800 (800 W 1600 mm/s).

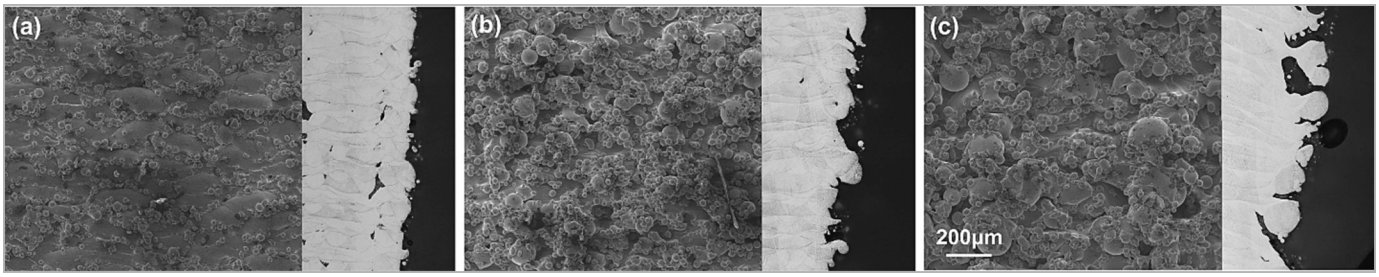

Fig. 11. Representative surface morphology by SEM on vertical surface and cross section view via optical microscopy under different process conditions. (a) ED2_P260 (260 W 1300 mm/s), (b) ED3_P620 (620 W 2067 mm/s), and (c) ED5_P800 (800 W 4000 mm/s).

tension, making the melt track smooth and clean. This further confirms that the solidified tracks and attached particles dominate the surface roughness at low energy density.

While in the case of ED5_P800 (Fig. 11(c) and Fig. 10(f)), large "droplets" stand out on the vertical surface in the cross-sectional view. They are well connected with the bulk. Note that those "droplets" are the semi-spheres seen in Fig. 10(f) and Fig. 11(c). Empty zones are also consistently observed around the large-sized semi-spheres. At the energy density group of 3 J/mm^2, shown in Fig. 11(b) and Fig. 10(e), for ED3_P620, some melt tracks are visible. Smaller-sized semi-spheres and partially remelted particles can be seen on the vertical surface, showing mixed features from the low and high energy density groups.

Representative regions on the vertical surfaces are further investigated with SEM for their microstructures. Fig. 12 shows the micrographs near the vertical surface for the case of ED2_P260. Under the relatively low magnification (Fig. 12(a)), a few particles are attached to the surface, and most of the regions are made of smooth melt tracks. Under the high magnification, cellular structures are observed, as shown in Fig. 12 (c) (in the bulk region) and Fig. 12(d) (close to the boundary), which exhibit similar primary dendritic arm spacing (PDAS). This suggests that the materials in bulk and close to the surface experienced similar cooling conditions. Fig. 12(b) shows the microstructure of an attached particle. The size and shape of the particle and the interface at the connecting area suggest that it is an attached powder. The cellular structure size in the powder is relatively larger than that in the bulk material, which is due to the gas atomization manufacturing process yielding a lower cooling rate than that in the L-PBF process [54].

Fig. 13 shows the microstructures of the case ED5_800 in the high energy density group. The large-sized droplet feature and its surrounding region are shown in Fig. 13(a). A similar feature has been observed on downfacing surfaces, which is defined as a "dross" [41]. Here a similar definition for those large-sized droplets was used in this study. Two distinguished regions of microstructures are observed between the bulk materials and the dross. The zoom-in areas are shown in Fig. 13(c) and (d). It is clearly demonstrated that larger sub-grains (cellular structures) are observed in the dross, indicating that it experiences a slower solidification environment during its formation process than the bulk material. The microstructures are inhomogeneous in the dross, as shown in Fig. 13(b) and Fig. 11(c). At the location close to the bulk material, the subgrains have a similar size to the bulk. The cellular size increases in the center of the dross and decreases again on the surface. Previous studies show that spatters, which have a larger subgrain size, can be a primary factor in surface roughness [55–57]. Meanwhile, a clear interface is expected between spatter and bulk material with distinguished microstructures without any transition. Therefore, a different forming mechanism is required to explain the dross formation on vertical surfaces.

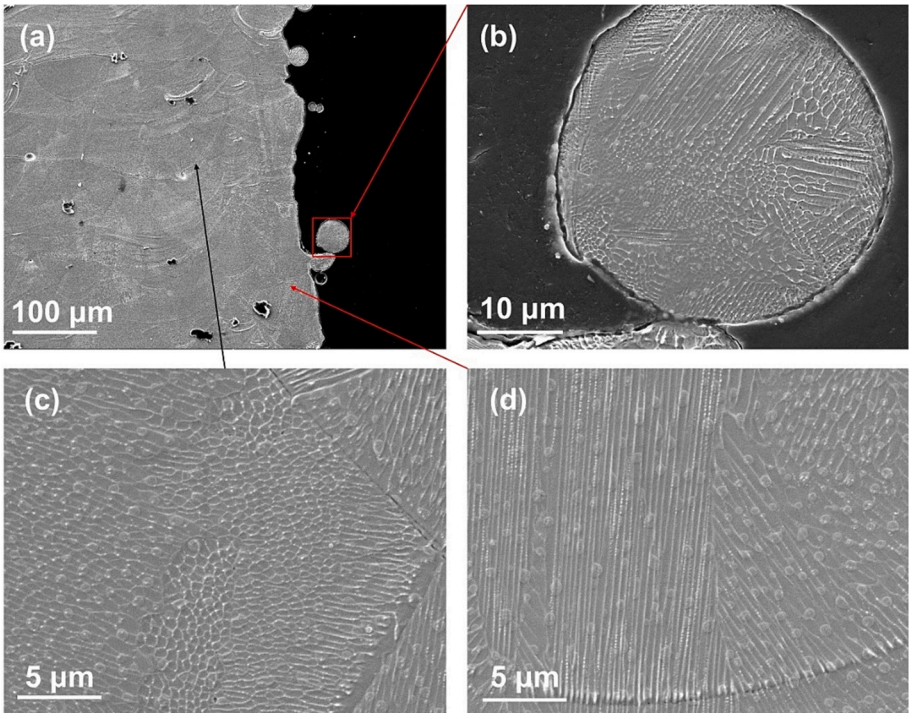

Fig. 12. Micrographs of the vertical surface for ED2_P260 (260 W 1300 mm/s) via SEM: (a) a selected representative region at the vertical surface. (b) zoom-in image for the attached particle. (c) microstructure in bulk materials, and (d) microstructure near the melt pool boundary.

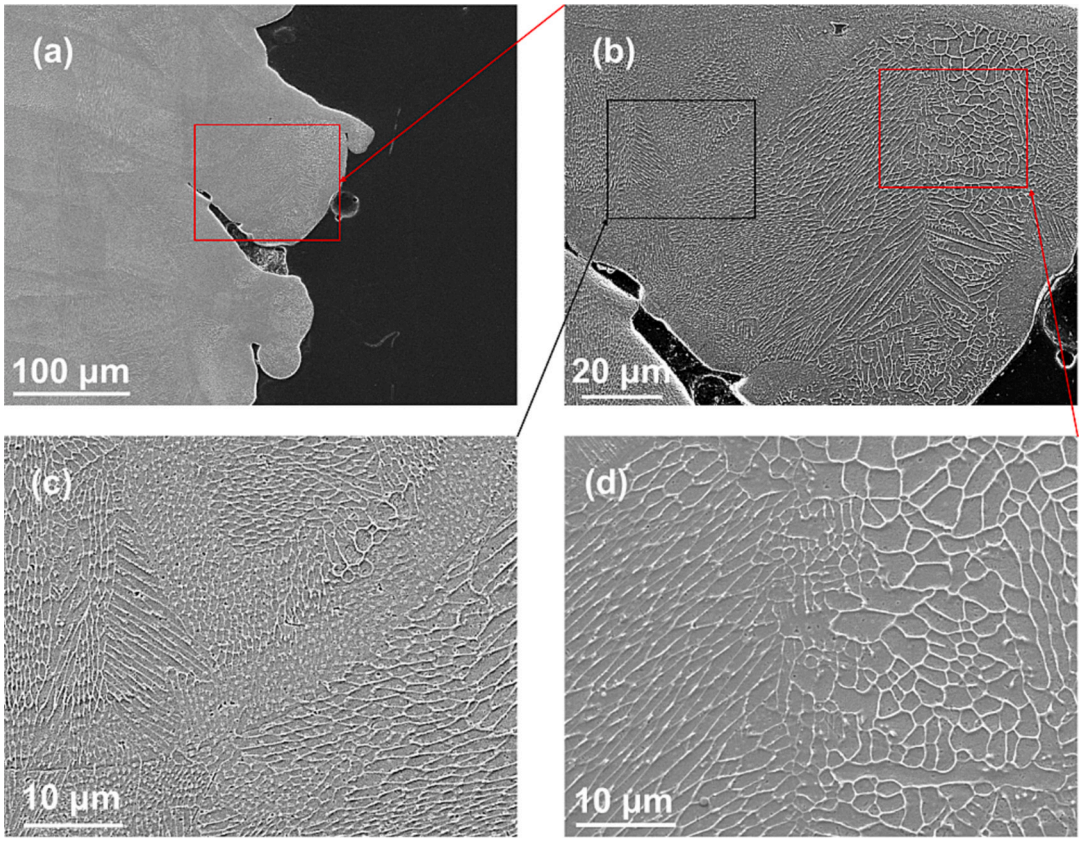

Fig. 13. Micrographs for the vertical surface for ED5_800 (800 W 1600 mm/s) by SEM: (a) dross on the vertical surface, (b) microstructure in the dross, (c) microstructure in the transition region between the dross and the bulk material, and (d) microstructure at the center of the dross.

3.3. Dross formation on the vertical surfaces

The dross formation has been exclusively reported only on downfacing surfaces. It typically evolves from a single melt pool track since the loose powder cannot support the melt pool. The extension of the melt pool forms dross. In addition, powders with low thermal conductivity promote melt pool expansion, further facilitating the dross formation [24,40,41]. However, dross formation on the vertical surface has not been reported and explained in the literature. The mechanisms of dross formation on the downfacing surface cannot directly explain the observations on vertical surfaces since the bottom of the melt pool does not directly face the powder. Based on the observations in Fig. 11 and Fig. 13, a mechanism grounded on a multi-layer melt pool instability is proposed here to explain the formation of dross on vertical surfaces, which is illustrated in Fig. 14.

When a laser scans a bulk region, the cross-section of a melt pool tends to have a symmetrical shape due to the homogenous heat transfer conditions (Fig. 14(a)). At the bulk-powder boundary, since the loose powders have much lower effective thermal conductivity [58], heat energy can accumulate at the powder side, leading to an asymmetry melt pool shape where the melt pool becomes deeper and larger towards the powder boundary (Fig. 14(b)). The surface tension has an inward cohesive force [59] in the melt pool. Therefore, under high energy density conditions, the conjunct powders can be drawn into the melt pool, making the powder around the melt pool less packed and creating a denudation zone between the melt pool track and the powder domain [60]. As the solidification process continues, the melt pool can shrink as temperature decreases, and the surface tension continues to work inward. As the melt pool absorbs powder and shrinks, the denudation zone exists aside from the vertical wall and partially under the melt track boundaries (Fig. 14(c)). As the printing process continues, the recoating process can bring new powder that may partially fill the denudation zone close to the side of the melt pool track, and the region below the melt track would remain empty. As the remelting continues, repeating the phenomena in Fig. 14(b), the large and deeper melt pools continue to expand to the powder region with the denudation zone keeps growing, shown in Fig. 14(c), which creates a scenario similar to a downfacing surface with an overhang staircase. After a few layers, as the vertical wall keeps pushing towards the powder with potentially a large denudation zone underneath the melt pool, the combination of the gravity (shown as G is Fig. 14(d)) and the recoil pressure due to vaporization of metal under high energy density (shown as P is Fig. 14(d)), working with the Marangoni force (shown as M in Fig. 14(d)) and surface tension (shown as δ in Fig. 14(d)), drive the outward melt pool instability and potentially form a droplet from the melt pool into the denudation zone and powder, shown as Fig. 14(e). As the melt pool extends into the powder, the high-temperature liquid could keep melting powders and growing larger. Since the additional materials absorb the heat to finish the phase transition as well as conduct away, the melt pool temperature decreases. The surface tension and viscosity are higher in a low-temperature environment, preventing the melt pool from further infiltration. Under the surface tension and gravity, spherical-shaped dross eventually forms without much support from powders, shown as a similar shape as observed in the experiment in Figs. 11 and 13. The shrinkage of the dross decreases the connecting area between the melt pool and powder, creating an isolated solidification environment for the dross on the powder side, as shown in Fig. 14(e). Since the dross is developed from the melt pool, the connected region would have a similar microstructure as the bulk in the melt pool. On the other hand, as the portion that is close to the powder experiences a lower cooling rate, a coarser microstructure is expected.

The primary dendrite arm spacing (PDAS) was measured based on the mean linear intercept method by ASTM E112 for the representative processing parameters. The PDAS measurements reflect the cooling condition the samples experienced: the larger the PDAS, the slower the cooling rate. As shown in Fig. 15, the case with higher energy density has larger PDAS in bulk, which is consistent with the cooling rate estimation under different laser power and speed using Rosenthal analytical solutions [61,62]. For ED5_P800, the PDAS has also measured at the connection region of dross and bulk, and the area inside the dross. The mean value of PDAS in the dross is 2.48 times larger than that in bulk with significant variation, implying that the cooling rate in the dross is

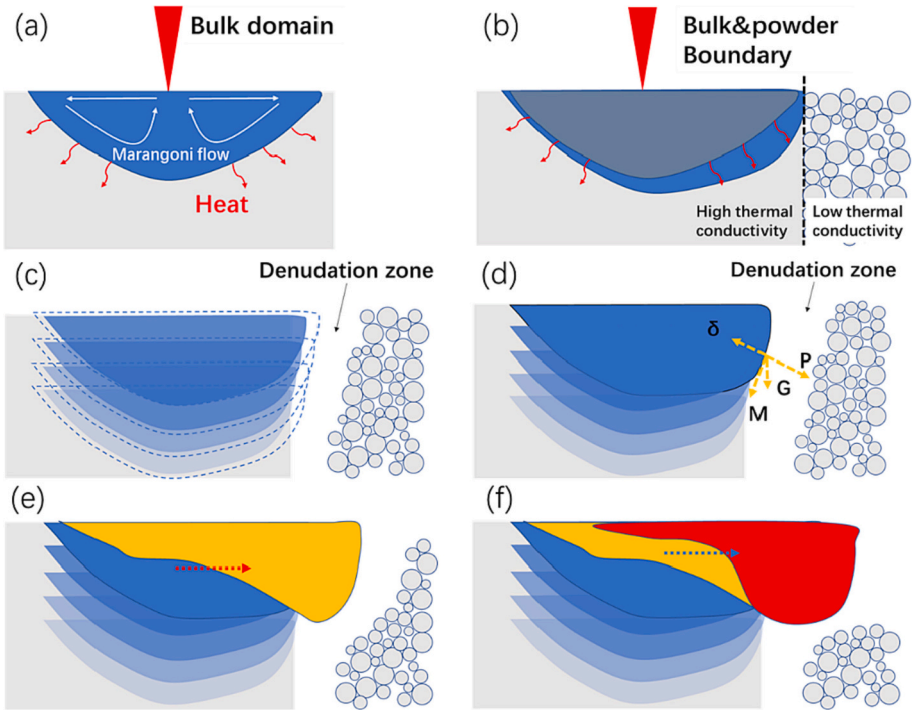

Fig. 14. Schematic of the dross formation on the vertical surface: (a) ideal melt pool shape in the bulk domain, (b) melt pool shape at the boundary, (c) the formation of denudation after multiple layers, (d) the force at the boundary of the melt pool, (e) the melt pool evolution, (f) dross formation.

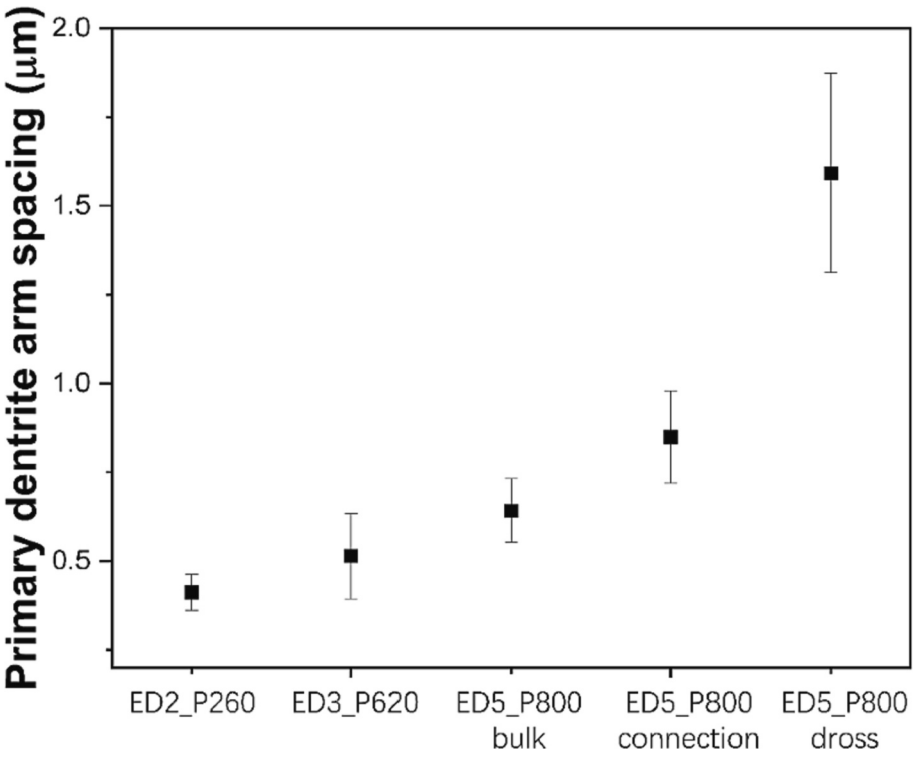

Fig. 15. Measured PDAS for selective process conditions.

much lower than the bulk material. While at the connection region between the dross and bulk material, the PDAS is rather similar, with slightly higher values. This suggests that the dross is developed from the melt tracks, experiencing similar cooling conditions as bulk. This indirectly confirms the proposed isolated thermal environment during the dross formation.

Since the dross significantly increases the roughness on vertical surfaces, preventing its formation is one of the effective means to improve the surface roughness. Based on the forming conditions and the mechanisms, the following methods can be proposed to deal with the dross on vertical surfaces: 1) apply low energy density for contour parameters: when the infill parameters are with high energy density, dross formation can be expected at the outmost region. Therefore, the low energy density contour parameters can melt and eliminate the dross evolved from the infill scans and improve the surface roughness. This has been a practice for contour parameters [38]. However, if the contour energy density is too low with insufficient melts, the lack of fusion may occur between the contour and bulk, and more partially remelted particles will appear; 2) increase the distance between contour and infill scans if high contour energy density parameters are required: This efficiently reduces the heat transfer from the contour to the bulk material, which prevents the asymmetric melt pool shape and stabilizes the melt pool, further decreases dross formation. However, if the distance between the contour and infill is set larger than the melt pool size, the contour melt track can't connect with the infill scans, which causes both the product dimension inaccuracy and rough surfaces; 3) alternate the distance between the contour and infill scans. This would break up the continuous expansion of the melt pool under high energy density conditions and prevent dross formation on the vertical surface.

4. Conclusions

The effects of energy density on surface roughness, in particular, for vertical surfaces, are investigated in this study. While examining the melt pool dimensions, surface topography, and microstructures for a wide range of process parameters, the correlation between the melt pool dynamics and the surface roughness is discussed. A new mechanism for dross formation under high energy density conditions on vertical surfaces, based on multi-layer melt pool instability, is proposed. The key conclusions are summarized as follows:

1. The top surface roughness increases with increasing power (speed) under the low energy density condition (2 J/mm^2) due to high melt pool instability and poor wetting condition. In contrast, it decreases with increasing power (speed) under the high energy density condition (5 J/mm^2) due to the larger remelt region, gravity and Marangoni flow. A smooth top surface (Sa $<$ 15 μm) can be achieved by applying laser power higher than 260 W with the energy density of 5 J/mm^2.
2. The vertical surface roughness is positively correlated with the melt pool dimensions (width and depth). Both increase with energy density under identical laser power or speed. Under equal energy density, they increase with increasing power or speed. In this study, a good vertical surface quality (Sa $<$ 15 μm) can be achieved by using laser power lower than 440 W with the energy density of 2 J/mm^2.
3. Partially remelted particles and melt tracks dominate the vertical surface roughness under the low energy density condition (2 J/mm^2). The dross dominates in the high energy density condition (5 J/mm^2). A mixture of these features exists in the intermediate energy density condition (3 J/mm^2).
4. The mechanism for dross formation on vertical surfaces is proposed: the low thermal conductivity of power and the existence of the denudation zone promote the melt pool extension towards the powder region. An empty zone can be formed by the denudation effect, and the Marangoni force, recoil pressure, and gravity work against the surface tension resulting in dross on vertical surfaces.

Since most of the study on surface roughness in L-PBF is on the top and the downfacing surfaces, this study fills the gaps by uncovering the factors that dominate the surface roughness on vertical surfaces. By revealing the dross formation mechanisms on vertical surfaces, effective methods can be further evaluated to control surface roughness. This also

provides a means to systematically optimize the L-PBF process parameters, not only the infill for bulk materials but also the contours at the surfaces. Continuing works have been developing computational models further to explain the surface roughness and performing experimental studies based on the proposed methods to improve the surface roughness.

CRediT authorship contribution statement

Tianyu Zhang: Conceptualization, Methodology, Formal analysis, Investigation, Writing – original draft, Writing – review & editing. **Lang Yuan:** Conceptualization, Methodology, Resources, Writing – review & editing, Supervision, Project administration, Funding acquisition.

Declaration of Competing Interest

The authors declare that they have no known competing financial interests or personal relationships that could have appeared to influence the work reported in this paper.

Data availability

Data will be made available on request.

Acknowledgments

The authors would like to acknowledge the support from the National Science Foundation under grant number 2029425, the South Carolina Space Grant Consortium under grant 521179-RP-SC007, and the National Aeronautics and Space Administration grant 20-EPSCoR2020-0068.

References

[1] T. DebRoy, et al., Additive manufacturing of metallic components – process, structure and properties, Prog. Mater. Sci. 92 (Mar. 2018) 112–224, https://doi.org/10.1016/j.pmatsci.2017.10.001.
[2] T.D. Ngo, A. Kashani, G. Imbalzano, K.T.Q. Nguyen, D. Hui, Additive manufacturing (3D printing): a review of materials, methods, applications and challenges, Compos. B. Eng. 143 (Jun. 2018) 172–196, https://doi.org/10.1016/J.COMPOSITESB.2018.02.012.
[3] D.L. Bourell, Perspectives on additive manufacturing, Annu. Rev. Mater. Res. 46 (1) (Jul 2016) 1–18, https://doi.org/10.1146/annurev-matsci-070115-031606.
[4] N.T. Aboulkhair, M. Simonelli, L. Parry, I. Ashcroft, C. Tuck, R. Hague, 3D printing of Aluminium alloys: Additive Manufacturing of Aluminium alloys using selective laser melting, in: Progress in Materials Science vol. 106, Elsevier Ltd, Dec. 01, 2019, p. 100578, https://doi.org/10.1016/j.pmatsci.2019.100578.
[5] S. Chen, Y. Tong, P. Liaw, Additive manufacturing of high-entropy alloys: a review, Entropy 20 (12) (Dec. 2018) 937, https://doi.org/10.3390/e20120937.
[6] N. Li, et al., Progress in additive manufacturing on new materials: A review, J. Mater. Sci. Technol. 35 (2) (Feb. 01, 2019) 242–269, https://doi.org/10.1016/j.jmst.2018.09.002. Chinese Society of Metals.
[7] J. Magnien, P. Cosemans, N. Nutal, T. Kairet, Current surface issues in additive manufacturing, Plasma Process. Polym. 17 (1) (Jan. 01, 2020) 1900154, https://doi.org/10.1002/ppap.201900154. Wiley-VCH Verlag.
[8] J.C. Snyder, K.A. Thole, Understanding laser powder bed fusion surface roughness, J. Manuf. Sci. Eng. Trans. ASME 142 (7) (2020), https://doi.org/10.1115/1.4046504.
[9] A. Townsend, N. Senin, L. Blunt, R.K. Leach, J.S. Taylor, Surface texture metrology for metal additive manufacturing: a review, Precis. Eng. 46 (Oct. 01, 2016) 34–47, https://doi.org/10.1016/j.precisioneng.2016.06.001. Elsevier Inc.
[10] J.H. Ryu, S.W. Nam, Effect of surface roughness on low-cycle fatigue life of Cr-Mo-V steel at 550 °C, Int. J. Fatigue 11 (6) (Nov. 1989) 433–436, https://doi.org/10.1016/0142-1123(89)90183-7.
[11] K.S. Chan, M. Koike, R.L. Mason, T. Okabe, Fatigue life of titanium alloys fabricated by additive layer manufacturing techniques for dental implants, Metall. Mater. Trans. A Phys. Metall. Mater. Sci. 44 (2) (2013) 1010–1022, https://doi.org/10.1007/s11661-012-1470-4.
[12] H. Rastan, A. Abdi, B. Hamawandi, M. Ignatowicz, J.P. Meyer, B. Palm, Heat transfer study of enhanced additively manufactured minichannel heat exchangers, Int. J. Heat Mass Transf. 161 (Nov. 2020), 120271, https://doi.org/10.1016/j.ijheatmasstransfer.2020.120271.
[13] Y. Zhu, et al., On friction factor of fluid channels fabricated using selective laser melting, Virtual Phys Prototyp 15 (4) (Oct. 2020) 496–509, https://doi.org/10.1080/17452759.2020.1823093.
[14] D.A. Lesyk, S. Martinez, B.N. Mordyuk, V.V. Dzhemelinskyi, Lamikiz, G. I. Prokopenko, Post-processing of the Inconel 718 alloy parts fabricated by selective laser melting: Effects of mechanical surface treatments on surface topography, porosity, hardness and residual stress, Surf. Coat. Technol. 381 (Jan. 2020) 125136, https://doi.org/10.1016/j.surfcoat.2019.125136.
[15] S.A. Khairallah, A. Anderson, Mesoscopic simulation model of selective laser melting of stainless steel powder, J. Mater. Process. Technol. 214 (11) (Nov. 2014) 2627–2636.
[16] I. Yadroitsev, I. Smurov, Surface morphology in selective laser melting of metal powders, Phys. Procedia 12 (PART 1) (2011) 264–270, https://doi.org/10.1016/j.phpro.2011.03.034.
[17] M. Yakout, A. Cadamuro, M.A. Elbestawi, S.C. Veldhuis, The selection of process parameters in additive manufacturing for aerospace alloys, Int. J. Adv. Manuf. Technol. 92 (5–8) (Sep. 2017) 2081–2098, https://doi.org/10.1007/s00170-017-0280-7.
[18] P.J. DePond, et al., In situ measurements of layer roughness during laser powder bed fusion additive manufacturing using low coherence scanning interferometry, Mater. Des. 154 (Sep. 2018) 347–359, https://doi.org/10.1016/j.matdes.2018.05.050.
[19] J.A. Cherry, H.M. Davies, S. Mehmood, N.P. Lavery, S.G.R. Brown, J. Sienz, Investigation into the effect of process parameters on microstructural and physical properties of 316L stainless steel parts by selective laser melting, Int. J. Adv. Manuf. Technol. 76 (5–8) (Feb. 2015) 869–879, https://doi.org/10.1007/s00170-014-6297-2.
[20] Z. Li, I. Kucukkoc, D.Z. Zhang, F. Liu, Optimising the process parameters of selective laser melting for the fabrication of Ti6Al4V alloy, Rapid Prototyp. J. 24 (1) (2018) 150–159, https://doi.org/10.1108/RPJ-03-2016-0045.
[21] Z. Chen, X. Wu, D. Tomus, C.H.J. Davies, Surface roughness of selective laser melted Ti-6Al-4V alloy components, Addit. Manuf. 21 (May 2018) 91–103, https://doi.org/10.1016/j.addma.2018.02.009.
[22] C. Qiu, C. Panwisawas, M. Ward, H.C. Basoalto, J.W. Brooks, M.M. Attallah, On the role of melt flow into the surface structure and porosity development during selective laser melting, Acta Mater. 96 (Jun. 2015) 72–79, https://doi.org/10.1016/j.actamat.2015.06.004.
[23] X. Shi, C. Yan, W. Feng, Y. Zhang, Z. Leng, Effect of high layer thickness on surface quality and defect behavior of Ti-6Al-4V fabricated by selective laser melting, Opt. Laser Technol. 132 (Dec 2020), https://doi.org/10.1016/j.optlastec.2020.106471.
[24] Y. Tian, D. Tomus, P. Rometsch, X. Wu, Influences of processing parameters on surface roughness of Hastelloy X produced by selective laser melting, Addit. Manuf. 13 (2017) 103–112, https://doi.org/10.1016/j.addma.2016.10.010.
[25] V. Alfieri, P. Argenio, F. Caiazzo, V. Sergi, Reduction of surface roughness by means of laser processing over additive manufacturing metal parts, Materials 10 (1) (2017), https://doi.org/10.3390/ma10010030.
[26] W.J. Sames, F.A. List, S. Pannala, R.R. Dehoff, S.S. Babu, The metallurgy and processing science of metal additive manufacturing, Int. Mater. Rev. 61 (5) (2016) 315–360, https://doi.org/10.1080/09506608.2015.1116649. Taylor and Francis Ltd.
[27] M.H. Nasab, D. Gastaldi, N.F. Lecis, M. Vedani, On morphological surface features of the parts printed by selective laser melting (SLM), Addit. Manuf. 24 (Dec. 2018) 373–377, https://doi.org/10.1016/j.addma.2018.10.011.
[28] G. Strano, L. Hao, R.M. Everson, K.E. Evans, Surface roughness analysis, modelling and prediction in selective laser melting, J. Mater. Process. Technol. 213 (4) (Apr. 2013) 589–597, https://doi.org/10.1016/J.JMATPROTEC.2012.11.011.
[29] J.C. Fox, S.P. Moylan, B.M. Lane, Effect of process parameters on the surface roughness of overhanging structures in laser powder bed fusion additive manufacturing, Procedia CIRP 45 (Jan. 2016) 131–134, https://doi.org/10.1016/J.PROCIR.2016.02.347.
[30] F. Kaji, A. Barari, Evaluation of the surface roughness of additive manufacturing parts based on the modelling of cusp geometry, IFAC-PapersOnLine 28 (3) (May 2015) 658–663, https://doi.org/10.1016/j.ifacol.2015.06.157.
[31] A. Triantaphyllou, et al., Surface texture measurement for additive manufacturing, Surf Topogr 3 (2) (2015) 24002, https://doi.org/10.1088/2051-672x/3/2/024002.
[32] D. Gu, Y. Shen, Balling phenomena in direct laser sintering of stainless steel powder: metallurgical mechanisms and control methods, Mater. Des. 30 (8) (Sep. 2009) 2903–2910, https://doi.org/10.1016/j.matdes.2009.01.013.
[33] I. Yadroitsev, A. Gusarov, I. Yadroitsava, I. Smurov, Single track formation in selective laser melting of metal powders, J. Mater. Process. Technol. 210 (12) (2010) 1624–1631, https://doi.org/10.1016/j.jmatprotec.2010.05.010.
[34] F. Calignano, D. Manfredi, E.P. Ambrosio, L. Iuliano, P. Fino, Influence of process parameters on surface roughness of aluminum parts produced by DMLS, Int. J. Adv. Manuf. Technol. 67 (9–12) (2013) 2743–2751, https://doi.org/10.1007/s00170-012-4688-9.
[35] J. Yang, et al., Role of molten pool mode on formability, microstructure and mechanical properties of selective laser melted Ti-6Al-4V alloy, Mater. Des. 110 (2016) 558–570, https://doi.org/10.1016/j.matdes.2016.08.036.
[36] N. Mumtaz, Hopkinson Kamran, Top surface and side roughness of Inconel 625 parts processed using selective laser melting, Rapid Prototyp. J. 15 (2) (2009) 96–103 (8).
[37] T. Yang, et al., The influence of process parameters on vertical surface roughness of the AlSi10Mg parts fabricated by selective laser melting, J. Mater. Process. Technol. 266 (Apr. 2019) 26–36, https://doi.org/10.1016/j.jmatprotec.2018.10.015.
[38] T. Yang, et al., Effect of processing parameters on overhanging surface roughness during laser powder bed fusion of AlSi10Mg, J. Manuf. Process. 61 (Jan. 2021) 440–453, https://doi.org/10.1016/j.jmapro.2020.11.030.

[39] X. Han, H. Zhu, X. Nie, G. Wang, X. Zeng, Investigation on selective laser melting AlSi10Mg cellular lattice strut: Molten pool morphology, surface roughness and dimensional accuracy, Materials 11 (3) (2018), https://doi.org/10.3390/ma11030392.
[40] A. Charles, A. Elkaseer, U. Paggi, L. Thijs, V. Hagenmeyer, S. Scholz, Down-facing surfaces in laser powder bed fusion of Ti6Al4V: effect of dross formation on dimensional accuracy and surface texture, Addit. Manuf. 46 (Oct. 2021), https://doi.org/10.1016/j.addma.2021.102148.
[41] A. Charles, M. Bayat, A. Elkaseer, L. Thijs, J.H. Hattel, S. Scholz, Elucidation of dross formation in laser powder bed fusion at down-facing surfaces: phenomenon-oriented multiphysics simulation and experimental validation, Addit. Manuf. 50 (Feb. 2022), https://doi.org/10.1016/j.addma.2021.102551.
[42] M.H. Nasab, D. Gastaldi, N.F. Lecis, M. Vedani, On morphological surface features of the parts printed by selective laser melting (SLM), Addit. Manuf. 24 (Dec. 2018) 373–377, https://doi.org/10.1016/J.ADDMA.2018.10.011.
[43] W.E. King, et al., Observation of keyhole-mode laser melting in laser powder-bed fusion additive manufacturing, J. Mater. Process. Technol. 214 (12) (2014) 2915–2925, https://doi.org/10.1016/j.jmatprotec.2014.06.005.
[44] J.A. Cherry, H.M. Davies, S. Mehmood, N.P. Lavery, S.G.R. Brown, J. Sienz, Investigation into the effect of process parameters on microstructural and physical properties of 316L stainless steel parts by selective laser melting, Int. J. Adv. Manuf. Technol. 76 (5–8) (Feb. 2015) 869–879, https://doi.org/10.1007/s00170-014-6297-2.
[45] J.P.M. Pragana, et al., Influence of processing parameters on the density of 316L stainless steel parts manufactured through laser powder bed fusion, Proc. Inst. Mech. Eng. B J. Eng. Manuf. 234 (9) (Jul. 2020) 1246–1257, https://doi.org/10.1177/0954405420911768.
[46] X. Nie, H. Zhang, H. Zhu, Z. Hu, L. Ke, X. Zeng, Analysis of processing parameters and characteristics of selective laser melted high strength Al-cu-mg alloys: from single tracks to cubic samples, J. Mater. Process. Technol. 256 (August 2017) 69–77, 2018, https://doi.org/10.1016/j.jmatprotec.2018.01.030.
[47] Y.S. Lee, W. Zhang, Modeling of heat transfer, fluid flow and solidification microstructure of nickel-base superalloy fabricated by laser powder bed fusion, Addit. Manuf. 12 (Oct. 2016) 178–188, https://doi.org/10.1016/j.addma.2016.05.003.
[48] K.C. Mills, B.J. Keene, Factors affecting variable weld penetration, Int. Mater. Rev. 35 (1) (1990) 185–216, https://doi.org/10.1179/095066090790323966.
[49] C.L.A. Leung, S. Marussi, M. Towrie, R.C. Atwood, P.J. Withers, P.D. Lee, The effect of powder oxidation on defect formation in laser additive manufacturing, Acta Mater. 166 (Mar. 2019) 294–305, https://doi.org/10.1016/j.actamat.2018.12.027.
[50] F. Calignano, D. Manfredi, E.P. Ambrosio, L. Iuliano, P. Fino, Influence of process parameters on surface roughness of aluminum parts produced by DMLS, Int. J. Adv. Manuf. Technol. 67 (9–12) (2013) 2743–2751, https://doi.org/10.1007/s00170-012-4688-9.
[51] I. Yadroitsev, A. Gusarov, I. Yadroitsava, I. Smurov, Single track formation in selective laser melting of metal powders, J. Mater. Process. Technol. 210 (12) (2010) 1624–1631, https://doi.org/10.1016/j.jmatprotec.2010.05.010.
[52] J.P. Kruth, L. Froyen, J. van Vaerenbergh, P. Mercelis, M. Rombouts, B. Lauwers, Selective laser melting of iron-based powder, J. Mater. Process. Technol. 149 (1–3) (2004) 616–622, https://doi.org/10.1016/j.jmatprotec.2003.11.051.
[53] F. Cabanettes, et al., Topography of as built surfaces generated in metal additive manufacturing: a multi scale analysis from form to roughness, Precis. Eng. 52 (December 2017) (2018) 249–265, https://doi.org/10.1016/j.precisioneng.2018.01.002.
[54] G.P. de León, V.E. Lamberti, R.D. Seals, T.M. Abu-Lebdeh, S.A. Hamoush, Gas atomization of molten metal: PartI. Numerical modeling conception, Am. J. Eng. Appl. Sci. 9 (2) (2016) 303–322, https://doi.org/10.3844/ajeassp.2016.303.322.
[55] I. Yadroitsev, P. Krakhmalev, I. Yadroitsava, S. Johansson, I. Smurov, Energy input effect on morphology and microstructure of selective laser melting single track from metallic powder, J. Mater. Process. Technol. 213 (4) (2013) 606–613, https://doi.org/10.1016/j.jmatprotec.2012.11.014.
[56] U. Ali, et al., Identification and characterization of spatter particles and their effect on surface roughness, density and mechanical response of 17-4 PH stainless steel laser powder-bed fusion parts, Mater. Sci. Eng. A 756 (April) (2019) 98–107, https://doi.org/10.1016/j.msea.2019.04.026.
[57] M.H. Nasab, D. Gastaldi, N.F. Lecis, M. Vedani, On morphological surface features of the parts printed by selective laser melting (SLM), Addit. Manuf. 24 (July) (2018) 373–377, https://doi.org/10.1016/j.addma.2018.10.011.
[58] M. Jamshidinia, F. Kong, R. Kovacevic, Numerical modeling of heat distribution in the electron beam melting® of Ti-6Al-4V, J. Manuf. Sci. Eng. Trans. ASME 135 (6) (2013) 1–14, https://doi.org/10.1115/1.4025746.
[59] S. Dong, et al., Research on metallurgical bonding of selective laser melted AlSi10Mg alloy, Mater. Res. Express. 7 (2) (2020), https://doi.org/10.1088/2053-1591/ab6dae.
[60] S.A. Khairallah, A.T. Anderson, A. Rubenchik, W.E. King, Laser powder-bed fusion additive manufacturing: physics of complex melt flow and formation mechanisms of pores, spatter, and denudation zones, Acta Mater. 108 (2016) 36–45, https://doi.org/10.1016/j.actamat.2016.02.014.
[61] L. Yuan, A.S. Sabau, D. Stjohn, A. Prasad, P.D. Lee, Columnar-to-equiaxed transition in a laser scan for metal additive manufacturing, IOP Conf. Seri. Mater. Sci. Eng. 861 (1) (Jun. 2020), https://doi.org/10.1088/1757-899X/861/1/012007.
[62] C.H. Ng, M.J. Bermingham, L. Yuan, M.S. Dargusch, Towards β-fleck defect free additively manufactured titanium alloys by promoting the columnar to equiaxed transition and grain refinement, Acta Mater. 224 (2022), https://doi.org/10.1016/j.actamat.2021.117511.